PAPER

Check for updates

Boosting the photocatalytic performance of Cu₂O for hydrogen generation by Au nanostructures and rGO nanosheets†

Yujie Ma, [ID] [a] Xindong Wei,[b] Kedeerya Aishanjiang,[c] Yi Fu,[a] Jiamei Le[a] and Hailong Wu*[a]

As a narrow band-gap semiconductor, cuprous oxide (Cu_2O) has a relatively high conduction band that can exhibit high driving force for the photocatalytic generation of hydrogen under visible light. Besides, its adjustable morphologies and abundant source also make it possible to be employed as a theoretically optimal photocatalyst. However, the low charge migration and poor stability commonly limit its practical application, and various strategies have been explored in previous studies. In this study, we have novelly utilized Au nanorod (NR) and nanobipyramid (NBP) nanocrystallites as well as rGO nanosheets to boost the photocatalytic activity of Cu_2O over hydrogen generation. The ternary rGO wrapped Au@Cu_2O with a yolk−shelled structure (y-Au@Cu_2O/rGO) was synthesized by a handy and controllable method. When excited by solar light (λ > 400 nm), it was found that the H_2 yields of Cu_2O/rGO, y-Au nanoparticle@Cu_2O/rGO, y-Au NR@Cu_2O/rGO, and y-Au NBP@Cu_2O/rGO were increased in the order of 248, 702, 1582 and 1894 μmol g^{-1} in 4 h. The outstanding photocatalytic performances of y-Au NR@Cu_2O/rGO and y-Au NBP@Cu_2O/rGO could be attributed to the combination function of quick electron transfer of rGO and abundant near-infrared-light-driven hot carriers on Au NRs and NBPs that could inject into Cu_2O and then a quick transfer to rGO to participate in H_2 reduction. Besides the above results, it was also found that Cu_2O maintained good stability after several cycling photocatalysis tests, which could be ascribed to the migration of holes from Cu_2O to Au that prevented the photooxidation of Cu_2O. This study may give a guide to fabricating controllable and effective photocatalysts based on plasmonic metals, semiconductors, or two-dimensional nanosheets, which possess full-solar-light-driven photocatalytic activities in the future.

1. Introduction

Photocatalysis is recognized as an alluring technology to solve energy and environmental crises because it can utilize inexhaustible solar energy to produce new chemical fuels.[1] Typically, we can gain renewable H_2 fuels from photocatalytic water splitting through the photocatalysis strategy, which has drawn increased attention over the past decades.[2,3] For the development of photocatalysis, the exploitation of efficient photocatalysts is of primary importance. Until now, various materials such as semiconductors, carbon materials, and transitional metal dichalcogenides have been studied as photocatalysts for

[a]Collaborative Innovation Center for Biomedicine, Shanghai University of Medicine & Health Sciences, Shanghai, 201318, China. E-mail: wuhl@sumhs.edu.cn

[b]ShuGuang Hospital Affiliated to Shanghai University of Chinese Traditional Medicine, Shanghai, 201203, China

[c]Department of Transplantation, Xinhua Hospital Affiliated to Shanghai Jiao Tong University School of Medicine, Shanghai, 200025, China

† Electronic supplementary information (ESI) available. See DOI: https://doi.org/10.1039/d2ra04132d

H_2 production.[3] Among these materials, semiconductors have always received considerable attention due to their easy fabrication, low cost, and nontoxicity to the environment.[4] Cuprous oxide (Cu_2O), as a p-type semiconductor, has a narrow band-gap ($\sim$2.17 eV) and relatively high conduction band and therefore possesses visible-light adsorption activity and high driving force for water splitting.[5,6] Thus, Cu_2O is theoretically considered an optimal material for the photocatalytic generation of H_2. However, in practical applications, the low photogenerated charge migration and poor stability restrict the further application of Cu_2O. To solve the low photocatalytic efficiency problem, various strategies, including regulating morphology, loading noble metals on Cu_2O, and combining Cu_2O with other semiconductors or carbon materials, have been widely employed in previous studies.[7–10] To solve the stability problem, these strategies could also be effective because the photogenerated oxidative holes in Cu_2O could be transferred and utilized quickly, driven by the built-in electric field between Cu_2O and the adjacent materials.

Among the above strategies, combining Cu_2O with plasmonic noble metals (Ag, Au, Cu) is the most direct strategy that

can obviously enhance the photocatalytic efficiency of Cu_2O.[11] On the one hand, the surface plasmon resonance (SPR) property of plasmonic noble metals could greatly improve the light absorption of Cu_2O. On the other hand, noble metals could accept the photogenerated charges from Cu_2O and transfer them quickly to the surroundings to be utilized. Besides, plasmonic noble metals could generate hot SPR charges under illumination to inject into Cu_2O to participate in the photocatalytic reaction, resulting in enhanced photocatalytic efficiency. Among these noble metals, Au nanorod (NR) and nanobipyramid (NBP) nanocrystallites have gained increasing attention due to their good chemical stability along with strong near-infrared SPR properties, which could enhance the near-infrared photocatalytic performance of Cu_2O and therefore make full-spectrum-driven photocatalysis viable.[12,13] For example, Yang *et al.* have reported a hot-dog-like Au NR@Cu_2O core–shelled composite, which showed high visible-light-driven photocatalytic activity.[14] Recently, our group has reported jujube-like Au NBP@Cu_2O core–shelled composites and yolk–shelled Au NR/NBP@Cu_2O composites, respectively, revealing these Au and Cu_2O composites possessed strong light absorption in the near-infrared region as well as full-spectrum-driven photocatalytic performance.[15,16] The stability of Cu_2O was also improved obviously due to the quick transfer of photogenerated holes to Au. Although the above Au NR/NBPs and Cu_2O composite photocatalysts showed considerable photocatalytic behaviour, there still existed a common problem that the photogenerated carriers on Cu_2O and hot carriers on Au are limited to some degree in the core–shelled structure that needed to be adequately transferred and separated in order to further boost the photocatalytic efficiency.

Reduced graphene oxide (rGO) has attracted much attention in recent years because of its fast electron transfer and has always served as the support material to improve the charge transfer of semiconductor photocatalysts.[17] Till now, Cu_2O/rGO composites have been studied widely, in which the presence of graphene could increase the charge transfer on Cu_2O and improve the stability of Cu_2O at the same time.[18,19] A few Cu_2O/graphene/plasmonic metal ternary composites have also been reported, revealing that the combination of rGO and plasmonic metals could together enhance the charge transfer and photocatalytic efficiency of Cu_2O.[20–22] However, there still lacks the combination of Au NR/NBP and rGO to improve the near-infrared-light-driven phtotocatalytic performance of Cu_2O and achieve full-spectrum-driven photocatalysis. Recently, Mahajan *et al.* have synthesized an Au NR-doped Cu_2O core–shell nanocube-embedded rGO composite that exhibited good photocatalytic degradation activity.[20] More studies about efficient Cu_2O/graphene/Au NR or Au NBP ternary composites that possess full-solar-spectrum response, fast photogenerated charge transfer on Cu_2O, and efficient hot charge utilization on Au need to be explored to obtain an alluring full-solar-spectrum-driven photocatalytic H_2 production.

In this study, we present ternary rGO-wrapped yolk–shelled Au@Cu_2O composites (Au@Cu_2O/rGO) by a simple and controllable method and explore their excellent H_2 generation activity under visible and near-infrared light. The Au NRs and NBPs used here could endow this composite with near-infrared light absorption, and their abundant hot carriers could endow them with near-infrared photocatalytic activity. This yolk–shelled Au@Cu_2O structure avoided the accumulation of hot carriers on Au, while the presence of rGO greatly increased the consumption of photogenerated charges. These advantages together led to an outstanding photocatalytic hydrogen activity over this y-Au@Cu_2O/rGO composites. This work may give a guide for the synthesis of efficient semiconductor/graphene/plasmonic metal ternary photocatalysts.

2. Experimental

2.1 Materials

Cuprous(II) chloride trihydrate ($Cu(NO_3)_2 \cdot 3H_2O$), hydrazine hydrate ($N_2H_4 \cdot H_2O$, 85% wt), cetyl trimethyl ammonium bromide (CTAB), chloroauric acid trihydrate ($HAuCl_4 \cdot 3H_2O$), ascorbic acid (AA), cetyl trimethyl ammonium chloride (CTAC), trisodium citrate (TSC), hydrogen chloride (HCl, 36% wt), hydrogen peroxide solution (H_2O_2, 30% wt), and ammonia solution ($NH_3 \cdot H_2O$, 25% wt) were purchased from Titan Chemicals (China). Sodium tetrahydroborate ($NaBH_4$) was purchased from Aladdin Chemicals (China). Silver nitrate ($AgNO_3$), poly(sodium-*p*-styrenesulfonate) (PSS, MW = 70 000), and polyvinyl pyrrolidone (PVP, MW = 50 000) were purchased from Sigma-Aldrich. All of these chemicals are analytically pure. Graphene oxide (GO, 1 wt%) was purchased from Dichuang (Suzhou) New Material Technology Co., Ltd. Deionized (DI) water with a resistivity of 18.2 MΩ cm was used in all experiments.

2.2 Photocatalyst preparation

The synthesis method of Au NPs, Au NRs, and Au NBPs can be found in the ESI.† For the synthesis of three rGO-wrapped Au@Cu_2O yolk–shelled composites (y-Au@Cu_2O/rGO), the dosage of Au NP/CTAB, Au NR/CTAB, and Au NBP/CTAB solutions used should be adjusted first to make their CTAB concentrations to be 0.1 M, and the optical densities were kept the same. Consider the synthesis of y-Au NR@Cu_2O/rGO, for example. Au NRs solution (20 mL, 0.1 M CTAB) was centrifuged at 7000 rpm for 10 min, and the sediment was dispersed in 20 mL of DI water. After sonication treatment, the above solution was dropped into PSS solution (2 g L^{-1}, 20 mL), including NaCl (6 mM). Stirring was continued overnight to link PSS on the CTAB stabilized Au NRs. After centrifugation at 6900 rpm for 10 min, the Au/PSS sediments were dispersed in 1 mL of DI water for subsequent use. Then, 1 mL of GO (1.0 wt%) was dispersed in 48.5 mL of DI water with sonication for 20 min. 1 g of PVP was added to the rGO solution and kept sonicating for another 20 min. 0.5 mL of $Cu(NO_3)_2$ solution (1.0 M) was dropped into the above solution under stirring, and after 10 min, the treated Au/PSS solution was added dropwise. It was kept stirring for a few minutes, and then 100 μL of $N_2H_4 \cdot H_2O$ ($V_{N_2H_4 \cdot H_2O} : V_{H_2O} = 1:1$) was injected into the above solution quickly. The products obtained at different reaction times (5, 30, 60, and 90 min) were centrifuged, washed with a mixture of

Paper

ethanol and water (1 : 1), and finally dried at 50 °C in a vacuum oven before characterization. For long-term storage, all the samples were stored in ethanol at 4 °C. The y-Au NP@Cu_2O/rGO and y-Au NBP@Cu_2O/rGO were synthesized with the same method except for replacing Au NRs with Au NP/PSS or Au NBP/PSS solutions. The rotation speeds used for Au NPs or Au NBPs solution were 8500 and 6800 rpm, respectively.

2.3 Photocatalytic activity measurement

2.3.1 Photocatalytic generation of H_2. 50 mg of the photocatalyst was suspended in 100 mL of Na_2S/$NaSO_3$ (0.35 M/0.25 M) solution for 20 min of sonication treatment. The suspension was bubbled with argon for 30 min before light irradiation. The measurement of photocatalytic generation of H_2 was carried out under visible and infrared light using a 300 W Xe arc lamp (PLS-SXE300UV, Beijing Perfect Light Co., Ltd) with a UV cut-off filter to cut off the light of wavelength less than 400 nm. The evolved H_2 was analyzed by gas chromatography, while argon was employed as the carrier gas.

2.3.2 Photocatalytic degradation of methyl orange (MO). The photocatalytic behaviour was evaluated by the degradation of MO in an aqueous solution under visible light irradiation ($\lambda >$ 400 nm). Typically, 5 mg of photocatalysts was dispersed in MO aqueous solution (30 mg mL^{-1}, 50 mL) by ultrasonic treatment. Then, the solution was stirred for 1 h in the dark to achieve adsorption–desorption equilibrium. After that, the photocatalytic measurement was carried out under visible and infrared light using a 300 W Xe arc lamp (PLS-SXE300UV, Beijing Perfect Light Co., Ltd) with a UV cut-off filter to cut off the light of wavelength less than 400 nm. After illumination, aliquots (5 mL) were taken out every 5 min and centrifuged to remove the photocatalytic particles. The absorption of the supernatant MO solution was determined spectrophotometrically at $\lambda_{max} = 464$ nm.

2.4 Electrochemical impedance spectroscopy (EIS) measurement

The samples with the same concentration were collected on cellulose membranes by suction filtration. Before testing, the cellulose membranes were pressed at 10 MPa for 1 min and cut into 0.5 × 0.5 cm pieces. A mixture containing 10 mM $K_3[Fe(CN)_6]$/$K_4[Fe(CN)_6]$ (1 : 1) and 0.5 M KCl was used as the electrolyte, while a Pt foil and Ag/AgCl electrode were used as the counter electrode and reference electrode, respectively. The EIS measurement was performed with an electrochemical workstation (CHI760E, Chenhua, Shanghai, China) in the frequency region from 10 MHz to 100 MHz and an AC amplitude of 5 mV at room temperature.

3. Results and discussion

As shown in Scheme 1, the rGO-wrapped yolk–shelled Au@Cu_2O composites with a different Au NP, Au NR, and Au NBP core were obtained by using a handy method, during which the yolk–shell was formed through Ostwald ripening process. This Ostwald ripening process has been demonstrated in our
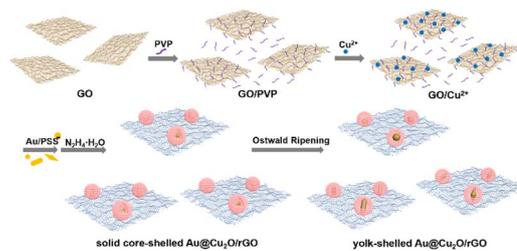
Scheme 1 Schematic illustration of the synthesis of Au@Cu_2O/rGO composites.

previous work on hollow Cu_2O as well as yolk–shelled Au@Cu_2O (Fig. S1†).[16] In this work, PVP was used as the dispersant for GO in the first stage. After adding the positive Cu^{2+}, it could adsorb on the negative GO surface through the electrostatic adsorption effect. The Au nanostructures stabilized with CTAB were treated with centrifugation and linked with negative PSS before use. The obtained negative Au/PSS was added to the GO and PVP solution and then could contact Cu^{2+} and form solid core–shelled Au@Cu_2O quickly after adding the reductant N_2H_4·H_2O. Meanwhile, part of GO could be reduced to rGO by N_2H_4·H_2O and wrapped on Au@Cu_2O. The interesting thing was the following Ostwald ripening process, from which the solid Au@Cu_2O/rGO could change into y-Au@Cu_2O/rGO with the reaction time. During this process, PVP was primarily important because it could serve as an inside-out hollowing reagent. With the reaction time, the aggregates located near the core with higher surface energy could easily dissolve than those in outer shells, resulting in cavities in Au@Cu_2O. The yolk–shelled structure will make charge transfer much faster on both Au core and Cu_2O than those on solid ones. In our previous work, we have already proved that yolk–shelled Au@Cu_2O could be obtained with this Ostwald ripening process and exhibit much better photocatalytic activities than solid Au@Cu_2O.[16] Accordingly, in this work, y-Au@Cu_2O/rGO must be preferred rather than the solid core–shelled Au@Cu_2O/rGO.
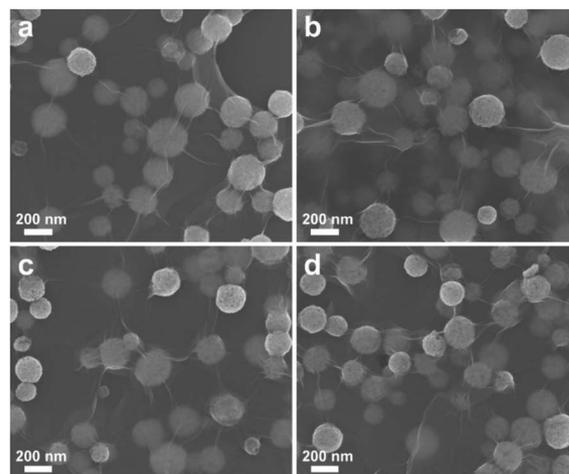

Fig. 1 (a–d) SEM images of Cu_2O/rGO samples obtained at 5, 30, 60, and 90 min, respectively.

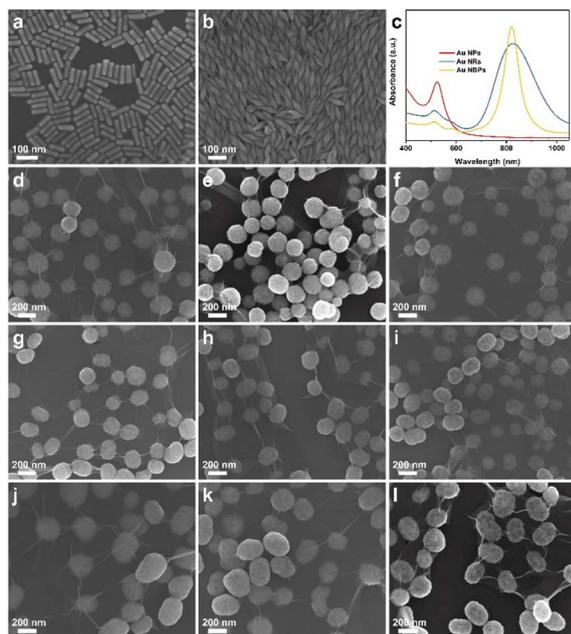© 2022 The Author(s). Published by the Royal Society of Chemistry

Fig. 2   SEM images of Au NRs (a) and NBPs (b). (c) UV-vis spectra of Au NPs, NRs and NBPs. (d–f) SEM images of Au NP@Cu$_2$O/rGO composites obtained at 5, 30, and 60 min, respectively. (g–i) SEM images of Au NR@Cu$_2$O/rGO composites obtained at 5, 30, and 60 min, respectively. (j–l) SEM images of Au NBP@Cu$_2$O/rGO composites obtained at 5, 30, and 60 min, respectively.

For investigating the synthesis process of rGO wrapped yolk–shelled structure, we took Cu$_2$O/rGO as an object of observation first. From Fig. 1, it can be seen that all the Cu$_2$O spheres are wrapped on rGO with an average size of 205 nm. TEM images in Fig. S2† show solid Cu$_2$O/rGO composites forming at the beginning 5 min. Hollow Cu$_2$O spheres wrapped on rGO occur at 60 min while part of the Cu$_2$O spheres breaks at 90 min. Accordingly, hollow Cu$_2$O/rGO obtained at about 60 min and y-Au@Cu$_2$O/rGO composites obtained at 60 min are employed as optimal samples in the following experiment. It is noted that there are some differences in the synthesis between y-Au@Cu$_2$O/rGO here and yolk–shelled Au@Cu$_2$O in our previous work.[16] Primarily, the dosage of PVP used in this work is doubled to that of yolk–shelled Au@Cu$_2$O. This is because there were some PVP molecules that must be used as the dispersant for GO in the first step, while the remaining PVP was employed as the inside-out hollowing reagent in the following Ostwald ripening process. The other difference between y-Au@Cu$_2$O/rGO and yolk–shelled Au@Cu$_2$O is that the existence of rGO slows down the Ostwald ripening process. The reason is that the diffusion of Cu^{2+} ions dissolved from aggregates located near the core with higher surface energy is hindered by the rGO coated on Cu$_2$O. As a result, the yolk–shelled structure in y-Au@Cu$_2$O/rGO was less obvious than that in yolk–shelled Au@Cu$_2$O, and the formation speed of the yolk–shelled structure was obviously stretched for y-Au@Cu$_2$O/rGO in this work.

The SEM and TEM images for Au NPs, NRs, and NBPs are shown in Fig. S3, S4,† and 2a and b, from which their length/diameter are measured as 20 nm, 80/40 nm, and 105/30 nm.

It can be found that Au NPs have a maximum SPR absorption peak at 520 nm while both Au NRs and Au NBPs have longitudinal transverse SPR absorption at 825 and 820 nm, respectively (Fig. 2c). The SEM images of Au NP@Cu$_2$O/rGO, Au NBR@Cu$_2$O/rGO, and Au NBR@Cu$_2$O/rGO composites obtained at 5, 30, and 60 min respectively are presented in Fig. 2d–l. The average sizes of these three Au@Cu$_2$O/rGO composites are 200 nm, 226 nm, and 260 nm, respectively. The morphology evolutions of these composites with reaction time are similar to that of Cu$_2$O/rGO. For these composites, Cu$_2$O spheres are solid at the beginning 5 min and become loose at 30 min and finally form a yolk–shelled structure at 60 min. All of the Au@Cu$_2$O composites are wrapped well on rGO, indicating the successful synthesis of the rGO-wrapped yolk–shelled Au@Cu$_2$O structure. In order to show the formation process of yolk–shelled structure clearly, TEM images of the three Au@Cu$_2$O/rGO composites obtained at 5, 20, 40, and 60 min, respectively, are shown in Fig. S5.† From these TEM images, it can be seen that the Cu$_2$O shell becomes thinner and Au core becomes clear with reaction time. The Cu$_2$O shell finally forms the yolk–shelled structure with a movable Au core at 60 min.

TEM images of y-Au NP@Cu$_2$O/rGO, y-Au NBR@Cu$_2$O/rGO, and y-Au NBR@Cu$_2$O/rGO are shown in Fig. 3a–c respectively, from which the yolk–shelled structure can be seen. For all the y-Au@Cu$_2$O/rGO composites, each Cu$_2$O sphere contains only one Au core. The morphology of y-Au NBP@Cu$_2$O/rGO was further demonstrated by HAADF-STEM. As shown in Fig. 3d, the cavity can be found between the Au NBP core and Cu$_2$O shell. The elemental mappings of Au NBP@Cu$_2$O/rGO in Fig. 3e and f demonstrate the distribution of Au and Cu elements, respectively. It can be seen that the Au element is distributed as a bipyramid-like core while Cu elements are distributed as the shell around the Au NBP core, and the C element is distributed as the support for the Au NBP@Cu$_2$O particle. The above results together indicate the synthesis of y-Au@Cu$_2$O/rGO composites.

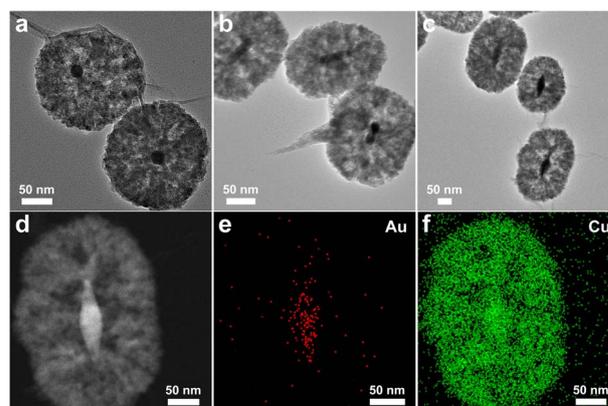The XRD pattern and Raman spectra were analyzed to investigate the phase purity and composition of these

Fig. 3   (a–c) TEM images of y-Au NP@Cu$_2$O/rGO, y-Au NR@Cu$_2$O/rGO, and y-Au NBP@Cu$_2$O/rGO, respectively. (d) HAADF-STEM image of the single y-Au NBP@Cu$_2$O/rGO particle. (e and f) Elemental maps of Au and Cu on the particle from (d).
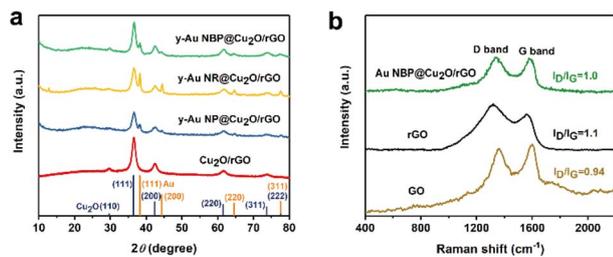
Fig. 4 (a) XRD patterns of Cu_2O/rGO, y-Au $NP@Cu_2O/rGO$, y-Au $NR@Cu_2O/rGO$, and y-Au $NBP@Cu_2O/rGO$ composites. (b) Raman spectra of GO, rGO, and Au $NBP@Cu_2O/rGO$.

composites synthesized in our work. The result in Fig. 4a shows that all the composites have peaks at 2θ of 24.2°, indicating the reduction of GO to rGO through the synthesis process.[19] For all the composites, it can be found that Cu_2O is clearly characterized *via* the main peaks at $2\theta = 29.6°$, 36.6°, 42.5°, 61.5°, 73.7°, and 77.6°, corresponding to the (110), (111), (200), (220), (311), and (222) planes of pure Cu_2O (JCPDS, 65-3288), respectively. For the three y-$Au@Cu_2O/rGO$ composites, there are four diffraction peaks at $2\theta = 38.1°$, 44.4°, 64.6°, and 77.6°, corresponding to the (111), (200), (220), and (311) planes of cubic-phase Au (JCPDS, 05-0667), respectively. In addition to the above, there are no other impurities like CuO or Cu in these composites. Furthermore, compared to the XRD spectra of the three y-$Au@Cu_2O/rGO$ samples, the Au peaks in y-Au $NP@Cu_2O/rGO$ are relatively weak because the crystallinity of Au NPs is smaller than Au NRs and NBPs obtained from the oriented growth. For Au y-$NR@Cu_2O/rGO$ and y-Au $NBP@Cu_2O/rGO$, the XRD peaks of Au NRs in y-Au $NR@Cu_2O/rGO$ are more obvious than those of Au NBPs in y-Au $NBP@Cu_2O/rGO$. It should be noted that the crystal faces on the side wall of Au NRs are {110} and {100}, while the Au NBPs are surrounded by high-index {711} facets. This means the facet on Au NBPs has a smaller interplanar distance and lower atomic density, leading to poor light reflection and diffraction. Therefore, the XRD peaks of Au NRs are more observable than those of Au NBPs. Raman spectra of GO, rGO, and y-Au $NBP@Cu_2O/rGO$ are shown in Fig. 4b. Two noticeable peaks located at 1342 and 1582 cm^{-1} of y-Au $NBP@Cu_2O/rGO$ are assigned to the D and G band of rGO, respectively. The D band represents sp^3 vibrational defects and the randomness of graphitic carbon defects, while the G band reveals the stretching of sp^2-hybridized carbon atoms and corresponds with the symmetric characteristics and crystalline nature of rGO.[17] Commonly, the intensity ratio of the D to G band (I_D/I_G) is used as a good indicator to characterize the defects and disorder in carbon-based materials. From Fig. 4b, the I_D/I_G is 0.94 for GO, 1.1 for rGO, and 1.0 for y-Au $NBP@Cu_2O/rGO$, which indicates that the y-Au $NBP@Cu_2O/rGO$ has fewer defects and a higher amount of sp^2 domains, or in other words, a higher degree of graphitization. This result also reveals the successful reduction of GO to rGO through the synthesis progress in our work.

The UV-vis absorption spectra were employed to investigate the light absorption and photocatalytic capacity of Cu_2O/rGO

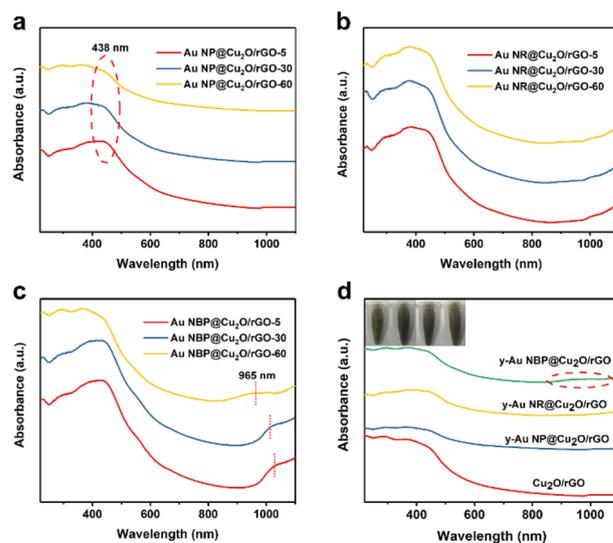**Fig. 5** (a–c) UV-vis spectra of Au $NP@Cu_2O/rGO$, Au $NR@Cu_2O/rGO$, and Au $NBP@Cu_2O/rGO$ composites obtained at 5, 30, and 60 min, respectively. (d) UV-vis spectra of Cu_2O/rGO, y-Au $NP@Cu_2O/rGO$, y-Au $NR@Cu_2O/rGO$, and y-Au $NBP@Cu_2O/rGO$ composites. The insert photos from left to right represent the solutions for the above four composites.

and the y-$Au@Cu_2O/rGO$ composites. As shown in Fig. 5, all of these composites have an obvious absorption band at about 438 nm, which belongs to the typical absorption capability of Cu_2O. The absorption band of Au NPs cannot be seen due to the interference of light scattering from the Cu_2O shell and rGO surrounding the Au core (Fig. 5a). Similarly, the absorption of Au NRs at the near-infrared region is also hidden and only presents an increased absorption trend at >900 nm region (Fig. 5b). But for Au $NBP@Cu_2O/rGO$, the absorption peak in the ~1000 nm region can be clearly seen, which belongs to Au NBPs. The presence of these peaks for Au $NBP@Cu_2O/rGO$ may be due to the much stronger SPR than both Au NRs and Au NPs. Compared with Au NBPs, the absorption peak for Au NBPs in Au $NBP@Cu_2O/rGO$ red shifts obviously mainly due to the high refractive index of Cu_2O surrounding Au NBPs.[12] Besides, it can be seen that the absorption peak for Au NBPs blue shifts with reaction time because the Cu_2O shell becomes thinner and the refraction of Cu_2O surrounding Au NBPs becomes weaker (Fig. 5c). The light absorption capabilities for Cu_2O/rGO and the three y-$Au@Cu_2O/rGO$ composites are compared as shown in Fig. 5d. It can be seen that all of the y-$Au@Cu_2O/rGO$ composites show obviously broader absorption in the visible light region. The insert photos in Fig. 5d from left to right represent Cu_2O/rGO, y-Au $NP@Cu_2O/rGO$, y-Au $NR@Cu_2O/rGO$, and y-Au $NBP@Cu_2O/rGO$ composite solutions, respectively. The color of these solutions changes from green to army green for the above four composites, indicating the broadening light absorption after adding Au NPs, Au NRs, and Au NBPs. Among the three y-$Au@Cu_2O/rGO$ composites, y-Au $NBP@Cu_2O/rGO$ shows an absorption band in the near-infrared region (>800 nm). All of the above results reveal that the y-$Au@Cu_2O/rGO$ composites have broadened light absorption in the visible region, which

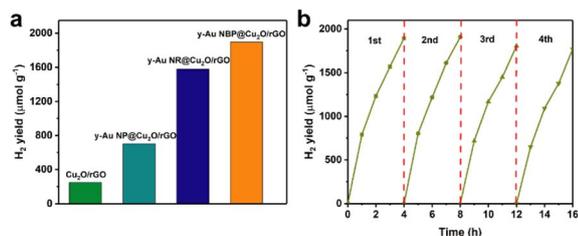**Fig. 6** (a) The photocatalytic H_2 yield of Cu_2O/rGO, y-Au NP@Cu_2O/rGO, y-Au NR@Cu_2O/rGO, and y-Au NBP@Cu_2O/rGO composites. (b) The cycling test for y-Au NBP@Cu_2O/rGO sample.

must lead to enhanced photocatalytic activities under visible light. Especially for Au NBP@Cu_2O/rGO, it may exhibit enhanced photocatalytic activity under near-infrared light.

The photocatalytic H_2 evolution activities of Cu_2O/rGO and y-Au@Cu_2O/rGO composites were then evaluated under visible light irradiation (>400 nm) *via* water splitting and are shown in Fig. S6.† We can see that the activities of y-Au NR@Cu_2O/rGO and y-Au NBP@Cu_2O/rGO are much higher and about seven times higher than Cu_2O/rGO and above two times higher than y-Au NPs@Cu_2O/rGO composites. Cu_2O/rGO shows the lowest H_2 yield of 248 μmol g^{-1} after 4 h because of its relatively poor photogenerated charge separation and utilization (Fig. 6a). The addition of Au NPs in Cu_2O/rGO leads to a higher H_2 yield of 702 μmol g^{-1}, which can be attributed to the hot carrier enhanced photocatalytic performance by the SPR property of Au NPs in the visible light region as well as the further charge transfer driven

by Au NPs. Compared with Cu_2O/rGO and y-Au NP@Cu_2O/rGO, y-Au NR@Cu_2O/rGO and y-Au NBP@Cu_2O/rGO exhibit much better photocatalytic activities with H_2 production of 1582 and 1894 μmol g^{-1} respectively, as a result of their broader light absorption and hot carrier enhanced photocatalytic capability by the SPR of Au both in the visible light and near-infrared light region. The y-Au NBP@Cu_2O/rGO possesses higher photocatalytic H_2 production than y-Au NR@Cu_2O/rGO due to the much stronger SPR of Au NBPs than that of Au NRs.[13] The above results agree well with the results of UV-vis spectra in Fig. 5. Table 1 presents the comparison of H_2 photogeneration for Cu_2O-based photocatalysts, from which we can see that our y-Au NR@Cu_2O/rGO and y-Au NBP@Cu_2O/rGO composites exhibit relatively higher photocatalytic abilities in H_2 production. In addition to the photocatalytic performance, stability is another indicator for efficient photocatalysts. Therefore, the cycling test for the y-Au NBP@Cu_2O/rGO sample was measured, as shown in Fig. 6b. It is revealed that the H_2 production rate only declines by 6.5% after four cycling tests, indicating the good stability of y-Au NBP@Cu_2O/rGO photocatalysts. We have also measured the XRD patterns of Cu_2O/rGO composites before and after photocatalysis and found no CuO components formed after photocatalysis (Fig. S8†), which again revealed the good stability of these composites. Furthermore, in order to demonstrate the photocatalytic activity of these composites, the photocatalytic degradation of MO over these composites was measured, as shown in Fig. S5.† It can be seen that y-Au NR@Cu_2O/rGO and y-Au NBP@Cu_2O/rGO possess much better activities than that of y-Au NP@Cu_2O/rGO and Cu_2O/rGO,

Table 1 Comparison of H_2 photogeneration for Cu_2O-based photocatalysts

Photocatalyst	H_2 yield (μmol g^{-1} h^{-1})	Light source	Sacrificial reagent	Ref.
Cu_2O/ZnO	21.6	300 W xenon lamp	Methanol (20 vol%)	23
Cu_2O/TiO_2	1388.3	—	Methanol (20 vol%)	24
Cu_2O/TiO_2-NF	48	200 W Hg–Xe arc lamp (plus a λ > 420 nm cut-off filter)	Water/ethanol mixture (0.5 mL, 1 : 1 v/v)	25
Cu_2O/rGO	352	200 W Hg–Xe arc lamp (plus a λ > 420 nm cut-off filter)	Methanol (10 vol%)	26
Cu_2O/rGO	10.7	300 W xenon lamp	Methanol (20%) aqueous solution	27
RGO–Cu_2O/Fe_2O_3	4.86	300 W xenon lamp (plus a λ > 420 nm cut-off filter)	Non	28
Cu_2O–rGO/TiO_2	3800	300 W xenon lamp	Methanol (20 vol%) and Pt (1.0 wt%)	29
rGO–Cu_2O/$BiWO_6$	1.8	Xenon lamp with a 420 nm cut-off filter	Non	30
Au/Cu_2O	153.5	300 W xenon lamp (plus a λ > 420 nm cut-off filter)	0.01 M NaOH and 0.0125 M glucose	31
Au NR/Cu_2O	105.1	300 W xenon lamp	0.01 M NaOH and 0.0125 M glucose	14
Cu/Cu_2O/rGO	125 200	300 W xenon lamp	Non	22
Cu_2O/rGO	62	300 W xenon lamp (plus a λ > 420 nm cut-off filter)	0.35 M/0.25 M, Na_2S/Na_2SO_3	This work
y-Au NP@Cu_2O/rGO	175.5	300 W xenon lamp (plus a λ > 420 nm cut-off filter)	0.35 M/0.25 M, Na_2S/Na_2SO_3	This work
y-Au NR@Cu_2O/rGO	395.5	300 W xenon lamp (plus a λ > 420 nm cut-off filter)	0.35 M/0.25 M, Na_2S/Na_2SO_3	This work
y-Au NBP@Cu_2O/rGO	473.5	300 W xenon lamp (plus a λ > 420 nm cut-off filter)	0.35 M/0.25 M, Na_2S/Na_2SO_3	This work
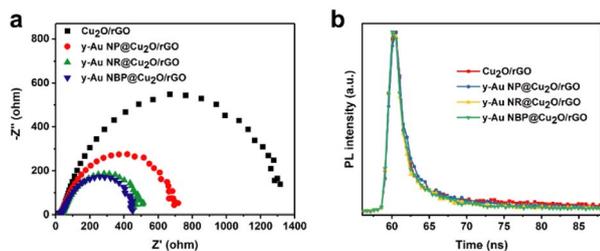
Fig. 7 (a) EIS measurements for Cu_2O/rGO, y-Au NP@Cu_2O/rGO, y-Au NR@Cu_2O/rGO, and y-Au NBP@Cu_2O/rGO composites. (b) TRPL spectra of Cu_2O/rGO, y-Au NP@Cu_2O/rGO, y-Au NR@Cu_2O/rGO, and y-Au NBP@Cu_2O/rGO composites.

Fig. 8 Schematic illustration of the possible photocatalysis mechanism of y-Au NBP@Cu_2O/rGO under solar light illumination.

which is consistent with the results of photocatalytic generation of H_2.

In order to investigate the charger transfer properties and explain the photocatalytic behavior for all the composites, electrochemical impedance spectroscopy (EIS) and time-resolved photoluminescence (TRPL) spectra were measured. For EIS measurement, the smaller diameter of the semicircle in the Nyquist plots represents smaller charge transfer resistance and better photocatalytic activity.[32] As shown in Fig. 7a, the diameter of the semicircle for Cu_2O/rGO, y-Au NP@Cu_2O/rGO, y-Au NR@Cu_2O/rGO, and y-Au NBP@Cu_2O/rGO gradually reduces, indicating the faster interfacial charge transfer after adding Au NPs, Au NRs, and Au NBPs successively. The y-Au NR@Cu_2O/rGO and y-Au NBP@Cu_2O/rGO composites show a much smaller diameter of the semicircle than Cu_2O/rGO and y-Au NP@Cu_2O/rGO, indicating their obvious capabilities to substantially enhance the photocatalytic activity. Moreover, y-Au NBP@Cu_2O/rGO possesses a slightly smaller diameter of the semicircle than y-Au NR@Cu_2O/rGO, which reveals that Au NBPs are more beneficial in improving the charge transfer in Cu_2O/rGO composites. The above results agree well with the photocatalytic behavior of these composites in Fig. 6a. The TRPL spectra were carried out to investigate the charge separation in the composites. As shown in Fig. 7b, all of the y-Au@Cu_2O/rGO composites show a short time constant when compared with Cu_2O/rGO, indicating the addition of Au can efficiently improve the charge transfer.[22] For the three y-Au@Cu_2O/rGO composites, the photoluminescence decay for y-Au NP@Cu_2O/rGO, y-Au NR@Cu_2O/rGO, and y-Au NBP@Cu_2O/rGO decrease in the order of 22.69, 20.67, and 14.67 ns (Table S1†), revealing the gradually better charger separation after adding Au NPs, Au NRs, and Au NBPs successively. The results from TRPL spectra also match well with the photocatalytic behavior in Fig. 6a. All of the above indicate the existence of Au can obviously improve the interfacial charge transfer and charge separation, and Au NRs, especially Au NBPs can make the maximal benefits to enhance the photocatalytic activity to the greatest extent.

Based on the above results and analysis, the photocatalytic mechanism for H_2 generation is given in Fig. 8. Here, consider y-Au NBP@Cu_2O/rGO as an example. Based on the work function of Cu_2O nanoparticles (4.3 eV) and Au NBP/NR (5.0 eV), electrons on Cu_2O will move to Au until the equilibrium of

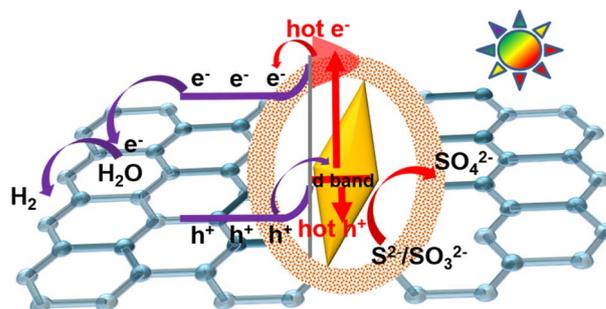Fermi energy level, resulting in the upward bend of Cu_2O and the formation of a built-in electric field. Under solar light ($\lambda >$ 400 nm), Cu_2O can be excited by visible light and produce photogenerated electrons and holes. The electrons transferred to the conduction band of Cu_2O can be then transferred quickly by rGO around Cu_2O to reduce water into H_2, while the holes on the valence band of Cu_2O can move to Au NBPs driven by the built-in electric field between Cu_2O and Au NBPs and then reduced by the sacrifice agent Na_2S/Na_2SO_3. Under solar light, Au NBPs will also be excited and generate hot electrons and holes because of their near-infrared SPR property. The hot electrons can inject into Cu_2O to participate in the reduction of water, while the hot holes can be consumed by Na_2S/Na_2SO_3. The holes on y-Au@Cu_2O/rGO can be consumed and maintain this redox reaction process to proceed continuously, which can be attributed to the yolk–shelled structure letting the charges transferred out/in unhindered. Additionally, Cu_2O can maintain good stability (Fig. 6) because the holes on Cu_2O can move to Au and also be efficiently consumed by Na_2S/Na_2SO_3. Based on the above advantages of y-Au NBP@Cu_2O/rGO, the y-Au NBP@Cu_2O/rGO composites exhibit outstanding H_2 photogeneration activity. The fourth charge transfer driven by Au NPs in the photocatalysis process is similar to that of Au NRs and Au NBPs. However, Au NPs can only absorb visible light and generate hot electrons and holes under visible light, and the amount of these hot charges is much smaller than those of Au NRs and NBPs due to the relatively weak SPR effect of Au NPs. This results in lower photocatalytic activity for y-Au NP@Cu_2O/rGO composites compared to y-Au NR@Cu_2O/rGO and y-Au NBP@Cu_2O/rGO composites. For Cu_2O/rGO composites without Au, only the photogenerated charges from Cu_2O can participate in the photocatalysis, leading to much lower photocatalytic activity over either H_2 production or MO degradation.

4. Conclusion

In this work, we developed a simple strategy to synthesize rGO-wrapped Au@Cu_2O composites with different Au nanocrystallites, in which the yolk–shelled Au@Cu_2O structures could be easily obtained with the increase in reaction time. It was significant to find that these novel y-Au@Cu_2O/rGO composites exhibited strong visible light absorption and

excellent photocatalytic activity for H₂ generation. Especially, y-Au NR@Cu₂O/rGO and y-Au NBP@Cu₂O/rGO composites showed unique near-infrared light absorption and exhibited about seven and two orders of magnitude higher photocatalytic generation of H₂ compared to Cu₂O/rGO and y-Au NP@Cu₂O/rGO, respectively. This can be attributed to the synergistic effects of quick electron transfer of rGO and abundant near-infrared hot carriers on Au NRs, especially on Au NBPs. This study provides a handy way to fabricate semiconductor, plasmonic metal, and nanosheet ternary photocatalysts, which may be helpful for the design of materials with full-spectrum-sunlight response for solar energy conversions.

Conflicts of interest

There are no conflicts to declare.

Acknowledgements

Notes and references

1 J. J. Zhang, H. G. Yu and J. G. Yu, Emerging S-scheme photocatalyst, *Adv. Mater.*, 2022, **34**, 2107668.

2 S. S. Chen, T. Takata and K. Domen, Particulate photocatalysts for overall water splitting, *Nat. Rev. Mater.*, 2017, 17050.

3 Q. Wang and K. Domen, Particulate photocatalysts for light-driven water splitting: mechanisms, challenges, and design strategies, *Chem. Rev.*, 2020, **120**, 919–985.

4 L. P. Zhang, J. R. Ran, S. Z. Qiao and M. Jaroniec, Characterization of semiconductor photocatalysts, *Chem. Rev.*, 2019, **48**, 5148–5206.

5 I. V. Bagal, N. R. Chodankar, M. A. Hassan, A. Waseem, M. A. Johar, D. H. Kim and S. W. Ryu, Cu₂O as an emerging photocathode for solar water splitting-A status review, *Int. J. Hydrogen Energy*, 2019, **44**, 21351–21378.

6 M. Muscetta, R. Andreozzi, L. Clarizia, I. D. Somma and Ra. Marotta, Hydrogen production through photoreforming processes over Cu₂O/TiO₂ composite materials: A mini-review, *Int. J. Hydrogen Energy*, 2020, **45**, 28531–28552.

7 S. Sun, X. Zhang, Q. Yang, S. Liang, X. Zhang and Z. Yang, Cuprous oxide (Cu₂O) crystals with tailored architectures: A comprehensive review on synthesis, fundamental

8 Z. H. Zhang, H. Wu, Z. Y. Yu, R. Song, K. Qian, X. Y. Chen, J. Tian, W. H. Zhang and W. X. Huang, Site-resolved Cu₂O catalysis in CO oxidation, *Angew. Chem.*, 2019, **131**, 4320–4324.

9 X. Deng, R. Li, S. Wu, L. Wang, J. Hu, J. Ma, W. Jiang, N. Zhang, X. Zheng, C. Gao, L. Wang, Q. Zhang, J. Zhu and Y. Xiong, Metal-organic framework coating enhances the performance of Cu₂O in photoelectrochemical CO₂ reduction, *J. Am. Chem. Soc.*, 2019, **141**, 10924–10929.

10 Y. S. Yuan, L. M. Sun, H. Gao, S. Mo, T. Y. Xu, L. Yang and W. W. Zhan, Engineering a highly improved porous photocatalyst based on Cu₂O by a synergistic effect of cation doping of Zn and carbon layer coating, *Inorg. Chem.*, 2020, **59**, 16010–16015.

11 L. N. Zhou, D. F. Swearer, C. Zhang, H. Robatjazi, H. Q. Zhao, L. Henderson, L. L. Dong, P. Christopher, E. A. Carter, P. Nordlander and N. J. Halas, Quantifying hot carrier and thermal contributions in plasmonic photocatalysis, *Science*, 2018, **362**, 69–72.

12 X. Z. Zhu, H. K. Yip, X. L. Zhuo, R. B. Jiang, J. L. Chen, X. M. Zhu, Z. Yang and J. F. Wang, Realization of red plasmon shifts up to ~900 nm by AgPd-tipping elongated Au nanocrystals, *J. Am. Chem. Soc.*, 2017, **139**, 13837–13846.

13 T. H. Chow, N. N. Li, X. P. Bai, X. L. Zhuo, L. Shao and J. F. Wang, Gold nanobipyramids: An emerging and versatile type of plasmonic nanoparticles, *Acc. Chem. Res.*, 2019, **52**, 2136–2146.

14 X. J. Yu, F. Z. Liu, J. L. Bia, B. Wang and S. C. Yang, Improving the plasmonic efficiency of the Au nanorod-semiconductor photocatalysis toward water reduction by constructing a unique hot-dog nanostructure, *Nano Energy*, 2017, **33**, 469–475.

15 Y. J. Ma, X. Z. Zhu, S. S. Xu, G. L. He, L. Yao, N. T. Hu, Y. J. Su, J. Feng, Y. F. Zhang and Z. Yang, Gold nanobipyramid@cuprous oxide jujube-like nanostructures for plasmon-enhanced photocatalytic performance, *Appl. Catal., B*, 2018, **234**, 26–36.

16 Y. J. Ma, X. Y. Liu, X. D. Wei, J. M. Le, Y. Fu, Q. Q. Han, H. L. Ji, Z. Yang and H. L. Wu, Yolk-shelled gold@cuprous oxide nanostructures with hot carriers boosting photocatalytic performance, *Langmuir*, 2021, **37**, 4578–4586.

17 A. Mondal, A. Prabhakaran, S. Gupta and V. R. Subramanian, Boosting photocatalytic activity using reduced graphene oxide (RGO)/semiconductor nanocomposites: issues and future Scope, *ACS Omega*, 2021, **6**, 8734–8743.

18 F. Z. Pu, Y. L. Bai, J. Lv, X. T. Zhao, G. C. Wu, C. C. Kong, B. Lei, X. J. Zhang, H. Jin and Z. M. Yang, Yolk–Shell Cu₂O@CuO-decorated RGO for high-performance lithium-ion battery anode, *Energy Environ. Mater.*, 2020, 1–8.

19 C. Chen, D. Li, A. Q. Wang, J. N. Guo, S. Dong, D. R. Chen, X. L. Jiao and Y. G. Xia, Interfacial enhancement for hydrogen radical transfer on hollow Cu₂O/rGO nanohybrid with efficient catalytic reduction activity, *Appl. Catal., A*, 2020, **590**, 117331.

20 H. Mahajan, S. K. Arumugasamy, A. Panda, V. Sada, M. Y. Yoon and K. Yun, Well-designed Au nanorod-doped Cu_2O core–shell nanocube-embedded reduced graphene oxide composite for efficient removal of a water pollutant dye, *ACS Omega*, 2020, **5**, 24799–24810.

21 J. N. Heo, J. Kim, J. Y. Do, N. K. Park and M. Kang, Self-assembled electron-rich interface in *defected* ZnO:rGO-Cu:Cu_2O, and effective visible light-induced carbon dioxide photoreduction, *Appl. Catal., B*, 2020, **266**, 118648.

22 N. Li, W. J. Yan, Y. Niu, S. J. Qu, P. P. Zuo, H. C. Bai and N. Zhao, Photoinduced *in situ* spontaneous formation of a reduced graphene oxide-enwrapped Cu-Cu_2O nanocomposite for solar hydrogen evolution, *ACS Appl. Mater. Interfaces*, 2021, **13**, 9838–9845.

23 Y. H. Zhang, X. L. Cai, Y. L. Li, M. M. Liu, C. L. Ding, J. L. Chen and S. M. Fang, Facile synthesis of hollow p-Cu_2O/n-ZnO microspheres with enhanced photocatalytic H_2 production, *Chem. Phys. Lett.*, 2019, **734**, 136748.

24 J. L. Chen, M. M. Liu, S. Y. Xie, L. J. Yue, F. L. Gong, K. M. Chai and Y. H. Zhang, Cu_2O-loaded TiO_2 heterojunction composites for enhanced photocatalytic H_2 production, *J. Mol. Struct.*, 2022, **1247**, 131294.

25 K. Sekar, C. Chuaicham, B. Vellaichamy, W. Li, W. Zhuang, X. H. Lu, B. Ohtani and K. Sasaki, Cubic Cu_2O nanoparticles decorated on TiO_2 nanofiber heterostructure as an excellent synergistic photocatalyst for H_2 production and sulfamethoxazole degradation, *Appl. Catal., B*, 2021, **294**, 120221.

26 S. Karthikeyan, K. Ahmed, A. Osatiashtiani, A. F. Lee, K. Wilson, K. Sasaki, B. Coulson, W. S. Aston, R. E. Douthwaite and W. Li, Pompon Dahlia-like Cu_2O/rGO nanostructures for visible light photocatalytic H_2 production and 4-chlorophenol degradation, *ChemCatChem*, 2020, **12**, 1699–1709.

27 Y. H. Zhang, X. L. Cai, D. Y. Guo, H. J. Zhang, N. Zhou, S. M. Fang, J. L. Chen and H. L. Zhang, Oxygen vacancies in concave cubes Cu_2O-reduced graphene oxide heterojunction with enhanced photocatalytic H_2 production, *J. Mater. Sci.: Mater. Electron.*, 2019, **30**, 7182–7193.

28 H. Q. Shen, G. W. Liu, X. Yan, J. H. Jiang, Y. Z. Hong, M. Yan, B. D. Mao, D. Li, W. Q. Fan and W. D. Shi, All-solid-state Z-scheme system of RGO-Cu_2O/Fe_2O_3 for simultaneous hydrogen production and tetracycline degradation, *Mater. Today Energy*, 2017, **5**, 312–319.

29 S. W. Hu, J. W. Shi, B. Luo, C. Q. Ai and D. W. Jing, Significantly enhanced photothermal catalytic hydrogen evolution over Cu_2O-rGO/TiO_2 composite with full spectrum solar light, *J. Colloid Interface Sci.*, 2022, **608**, 2058–2065.

30 H. Q. Shen, G. W. Liu, Y. Zhao, D. Li, J. H. Jiang, J. R. Ding, B. D. Mao, H. Shen, K.-S. Kim and W. D. Shi, Artificial all-solid-state system by RGO bridged Cu_2O and Bi_2WO_6 for Z scheme H_2 production and tetracycline degradation, *Fuel*, 2020, **259**, 116311.

31 B. Ma, J. L. Bi, J. Lv, C. C. Kong, P. X. Yan, X. T. Zhao, X. J. Zhang, T. Yang and Z. M. Yang, Inter-embedded Au-Cu_2O heterostructure for the enhanced hydrogen production from water splitting under the visible light, *Chem. Eng. J.*, 2021, **405**, 126709.

32 K. Le, X. Zhang, Q. Zhao, Y. Z. Liu, P. Yi, S. S. Xu and W. M. Liu, Controllably doping nitrogen into 1T/2H MoS2 heterostructure nanosheets for enhanced supercapacitive and electrocatalytic performance by low-power N2 plasma, *ACS Appl. Mater. Interfaces*, 2021, **13**, 44427–44439.